Article

Electrochemiluminescence Energy Resonance Transfer System between RuSi Nanoparticles and Hollow Au Nanocages for Nucleic Acid Detection

Haijie Lu, Jianbin Pan, Yinzhu Wang, Si-Yuan Ji, Wei Zhao, Xiliang Luo, Jing-Juan Xu, and Hong-Yuan Chen

Anal. Chem., **Just Accepted Manuscript** • DOI: 10.1021/acs.analchem.8b02347 • Publication Date (Web): 03 Aug 2018

Electrochemiluminescence Energy Resonance Transfer System between RuSi Nanoparticles and Hollow Au Nanocages for Nucleic Acid Detection

Hai-Jie Lu[1], Jian-Bin Pan[1], Yin-Zhu Wang[1], Si-Yuan Ji[1], Wei Zhao[1], Xi-Liang Luo[2], Jing-Juan Xu[1]*, Hong-Yuan Chen[1]*

[1]State Key Laboratory of Analytical Chemistry for Life Science and Collaborative Innovation Center of Chemistry for Life Sciences, School of Chemistry and Chemical Engineering, Nanjing University, Nanjing 210023, China

[2]Key Laboratory of Sensor Analysis of Tumor Marker, Ministry of Education, College of Chemistry and Molecular Engineering, Qingdao University of Science and Technology, Qingdao 266042, China

*: Corresponding author. Tel/Fax: +86-25-89687294; Email address:

weizhao@nju.edu.cn (W. Zhao) xujj@nju.edu.cn (J.J. Xu)

ABSTRACT:

This paper describes an electrochemiluminescence resonance energy transfer (ECL-RET) system using $Ru(bpy)_3^{2+}$-doped silica nanoparticles (RuSi NPs) as the ECL donor and hollow Au nanocages as the ECL acceptor. Tetrahedron DNA (TD) was used to construct the biosensing interface and control the distance (4.8 nm) between the ECL donor-acceptor pairs. The surface plasmon resonance (SPR) nanostructures, Au nanocages were assembled via the hairpin based sandwich assay. Due to the well overlap between the plasmon absorption spectrum of Au nanocages (628 nm) and the ECL emission spectrum of RuSi NPs (620 nm), high efficient energy transfer could occur. Subsequent cyclic DNA amplification further increased the binding amount of Au nanocages. Since the ECL inhibition is closely related with the binding amount of Au nanocages, a general "signal-off" ECL bioassay could thus be tailored with high sensitivity. At the optimized conditions, this ECL-RET system performed well with great stability and repeatability for nucleic acid detection in the range from 1.0 fM to 10 pM. This work manifested the great promise of hollow Au nanocages for an ECL-RET biosensor that to the best of our knowledge has not been reported. We believe that it could inspire more interest in the design and development of numerous other SPR nanostructures for advanced ECL-RET biosensors.

KEYWORDS: Gold nanocages, RuSi NPs, Tetrahedron DNA, Resonance energy transfer, Electrochemiluminescence

INTRODUCTION

Noble metal nanoparticles have received great interest in catalysis,[1] optical sensing[2,3] and biology[4,5] due to their unique optical and physical properties. Their optical properties result from the localized surface plasmon resonance (LSPR) which involves the coherent oscillation of the metal electrons in resonance with an incident light.[6-8] This oscillation induced strong surface electromagnetic fields.[9,10] In the past few decades, solid Au nanoparticles have been widely investigated in many biological applications.[11-14] These nanoparticles (for example, Au nanospheres) have surface plasmon fields only surrounding their surface.[15] Recently, hollow Au nanocages which possess two types of surface, one facing the outside and the other within the cavity have been studied.[16,17] Upon irradiation, electromagnetic field could occur at the inner and outer surface of Au nanocages.[18,19] The interaction between the excited magnetic fields leads to the observed red-shift in the plasmon band which is like the interaction between the fields of two plasmonic particles depending on their separation.[20] As a result of the empty design, hollow Au nanocages have the tunability of their surface plasmon resonance spectra in visble and near-IR regions which made the nanostructures intriguing in many fields such as photothermal therapy and other biomedical applications.[21-25]

Electrochemiluminescence resonance energy transfer (ECL-RET) is a spectroscopy method that is caused by the energy transfer between ECL donor and acceptor at the nanometer-scale.[26-32] At large distance, typically over 12 nm, the ECL-RET using the SPR structures as ECL acceptor could increase the emission intensity of the ECL

donor which was reported as "plasmon-enhanced ECL" in the previous literature.[33,34] At small distance, typically less than 10 nm, the ECL-RET mainly manifested as the quenching to the ECL signal.[35,36] Because of the unique advantages of ECL-RET, such as no interference from the scattering light, low cost and high sensitivity, ECL-RET has attracted growing attention in the detection of proteins, DNA and small molecules.[37-42] However, challenges exist in the system including the electrochemical instability of acceptor and the difficulty to find a well-overlapped ECL donor-acceptor pairs. In recent decades, plasmonic nanoparticles (Au, Ag, Pt nanoparticles) have been widely investigated as the acceptor in the ECL-RET system for their easy preparation and favorable electrochemical stability.[43,44] As a typical plasmonic nanostructure, gold nanospheres could exhibit high energy transfer efficiency to the ECL donor, for example semiconductor nanocrystals, in the ECL-RET biosensors due to its strong plasmon absorption.[45] Despite of the advantages, gold nanospheres are solid nanostructures and have constant electromagnetic field at a given size. These properties made it difficult to regulate the plasmon absorption band which limited its applications in the ECL-RET systems. Gold nanocages, as a hollow plasmonic nanostructure, have the tunability of their LSPR absorption band in the visible and near-infrared regions.[46] Moreover, gold nanocages possess a large absorption cross-section which increased their absorption efficiency towards the incident light.[47] Thus, gold nanocages could be a good acceptor candidate in the ECL-RET.

Herein, we report an ECL-RET system using $Ru(bpy)_3^{2+}$-doped silica nanoparticles (RuSi NPs) as the ECL donor and hollow gold nanocages as the ECL acceptor for the

detection of miRNA141. In our study, tetrahedron DNA (TD) was anchored on the surface of the electrode which provided the solution-phase-like environment[48] and regulated the distance (4.8 nm) between donor-acceptor pairs for the ECL energy transfer process. Target miRNA141 was introduced via the hybridization with the stem-loop structure of the TD vertex (hairpin 1). After incubated with the signal probe, hairpin 2 modified Au nanocages, the ECL-RET system was constructed. Because of the well overlap between the UV-vis absorption spectrum of Au nanocages (628 nm) and ECL emission spectrum of RuSi NPs (620 nm), high efficient energy resonance transfer could occur and ECL signal could be significantly quenched. Besides, the subsequent DNA cyclic amplification could increase the binding amount of the Au nanocages, which amplified the quenching signal and increased the detection sensitivity. On the basis of the forementioned technique, we studied the morphology and spectra effect of the ECL acceptor to the efficiency of ECL-RET using two kinds of Au nanoparticles with the same size of 18 nm, hollow Au nanocages and solid Au nanospheres. As a conventional sensing interface, single strand DNA (ssDNA) based interface was also used in this assay for the comparative study to the TD based sensing interface. Finally, under the optimization conditions, this ECL-RET system was used for the sensitive and specific detection of miRNA141, a recently discovered biomarker for prostate cancer with the detection limit at the fetomolar level. This proposed ECL-RET platform shows great promise in the clinical diagnosis.

EXPERIMENTAL SECTION

Reagents and Apparatus. Chemical reagents and apparatus are shown in the Supporting Information. Table S1 lists all the DNA and miRNA sequences used in this work.

Synthesis and Modification of RuSi NPs. The RuSi NPs were prepared according to the previous literature.[49,50] First, 1.77 mL of Triton X-100, 7.5 mL of cyclohexane, 1.8 mL of 1-hexanol, and 340 μL of $Ru(bpy)_3^{2+}$ (40 mM) were mixed with magnetic stirring at 300 rpm to form the water-in-oil microemulsion. After adding 100 μL of tetraethylorthosilicate (TEOS) and 60 μL of NH_4OH, the hydrolysis reaction was allowed to continue for 24 h. Next, acetone was added to destroy the emulsion, followed by centrifuging and washing with ethanol and water. The obtained orange-colored RuSi NPs were treated with 10% APTES alcoholic solution for 2 h to form amino group functionalized RuSi NPs. The nanoparticles were then rinsed with ethanol to remove loosely bound APTES and redispersed in ultrapure water.

Preparation and characterization of tetrahedron DNA (TD). TD was synthesized by the following procedure.[51] Equimolar quantities of four strands (S1, S2, S3, S4) for the formation of the tetrahedron were mixed in buffer (20 mM Tris, 50 mM $MgCl_2$, pH 8.0) at 95 ℃ for 10 min and then cooled to 4 ℃ in 30 s using a Peltier thermal cycler. After that, the TD nanostructure was formed and stored at 4 ℃ for use. The formation of TD in solution was confirmed through native-PAGE gel electrophoresis. In detail, different DNA structures (S1, S2, S3, S1S2, S2S3, S1S2S3, and S1S2S3S4) were all placed at 95℃ for 10 min and then cooled to 4 ℃ in 30 s.

Then, the gel electrophoresis was performed by injecting the loading samples (the mixture of different DNA structures, UltraPower TM dye and loading buffer) into a native polyacrylamide gel (8%). The loading samples were placed for 3 min and then injected into polyacrylamide hydrogel. The electrophoresis analysis was carried out at 150 V for 50 min and then the resulting board was observed under UV irradiation. Finally, Molecular Imager Gel Doc XR was applied to the photograph. To determine the yield of the TD assembly, the TD product was run on an 8% native gel and stained with Gel Red (Molecular Probes/Keygen Biotech). Using a Gel Doc XR Molecular Imager (Bio-Rad) and Quantity One analysis software (Bio-Rad), the ratio between the intensity of the TD band and the total intensity in the lane (minus the background) was determined and recognized as the yield of TD.

Synthesis of Target DNA-Au nanocages nanocomposite. The tDNA-Au nanocages nanocomposite was fabricated by the surfactant-assisted method.[52-54] To 1 mL of 2 nM purchased 18-nm Au nanocages solution, 10 μL of 1 wt% Tween 20 and 50 μL of 4 μM mPEG-SH (MW ~5 kDa) were added. After brief mixing, 8 μL of 100 μM deprotected thiolated DNAs was added to the mixture and 212 μL of 3 M NaCl was added to reach a final concentration of 500 mM. After aging for 60 min at room temperature, excess reagents were removed via centrifugation at 8000 rpm for 10 min. The precipitate was washed three times with 0.1 M PBS solution by repetitive centrifugation and dispersion. The obtained nanocomposite was redispersed in 1 mL of 0.1 M PBS solution and stored at 4 ℃ for use.

Fabrication of the ECL biosensor. The bare GCE was polished in sequential order with 1.0, 0.3, and 0.05 μm alumina slurry to obtain a mirror-like surface, followed by sonication in the ultrapure water and ethanol in turn, and finally, dried in air. First, 50 μL of chitosan and the prepared RuSi solution were mixed homogeneously by ultrasonic for 5 min. The CS-RuSi composite film was achieved by dropping 5 μL of the obtained RuSi solution onto the pretreated surface of GCE and evaporated in air at 37 ℃. Then, the CS-RuSi modified GCE was immersed in 50 μL of 2.5% (v/v) glutaraldehyde (GA) in PBS for 2 h of incubation at 37 ℃. Rinsed with 1x PBS thoroughly, the electrode was immersed in 50 μL of TD probes and incubated at 37 ℃ for 1 h. The TD modified electrode was blocked by 2 wt % BSA solution at 37 ℃ for 1 h and carefully rinsed with 1x PBS. Subsequently, different concentrations of target miRNA were incubated at 37 ℃ for 2 h. Then, 50 μL of tDNA-Au nanocages nanocomposite was dropped onto the surface of the electrode and incubated at 37 ℃ for 2 h. After that, the prepared electrode was washed with 1x PBS thoroughly for the follow-up ECL characterization. Each step of the assembly process was characterized by ECL measurement. The ECL signal of the electrode was recorded in 1x PBS containing 25 mM TprA.

RESULT AND DISCUSSION

Characterization of the RuSi NPs and Au nanocages. Figure 1A shows the SEM image of the synthesized RuSi NPs. According to the SEM observation, the

as-prepared RuSi NPs displayed good dispersion and uniform spherical shape with an average diameter of 60 nm. The nanoparticles were then mixed with chitosan (CS) to create a uniform film on the glass carbon electrode (CGE) surface. ECL emission of the CS-RuSi film was investigated which showed relatively strong intensity. As shown in Figure 1C, driving by the cyclic voltammetry from 0 ~ 1.25 V (a, black line), ECL of the RuSi NPs reached the peak at the potential of 1.2 V (b, blue line). Figure 1B displays the TEM image of Au nanocages at 100 nm and 10 nm scale (inset). It can be seen that the Au nanocages were hollow and porous nanostructure with an average size of 18 nm. The UV-vis spectrum of Au nanocages was characterized and shown in Figure 1D. A wide absorption peak centered at 628 nm was observed which belongs to the plasmon resonance absorption (a, black line). Upon irradiation, Au nanocages could excite electromagnetic field at the inner and outer surface of the hollow nanocage. The interaction between the excited magnetic fields leads to the observed red-shift in the plasmon band. This is like the interaction between the fields of two plasmonic particles. As shown in Figure S1, the FDTD simulations of the cross-section of Au nanocages exhibited enhanced electromagnetic field (A) and the red-shift scattering peak (B) at 630 nm. Since the ECL emission peak of RuSi NPs was 620 nm (b, blue line), which overlapped well with the plasmon absorption band of Au nanocages, the ECL signal of RuSi NPs could be significantly quenched at appropriate distance during the ECL detection process.

Gel analysis of the TD. To confirm the successful assembly of TD after annealing, gel electrophoresis (PAGE) was performed.[55] As seen in Figure 2, compared with the

combinations of three strands (lanes 6) and the single strand DNA (lane 4~5), TD (lane 7) showed slower mobility. For TD, the difference of migrating rate was attributed to the spatial complexity and increased mass, which hindered the movement through the pores of polyacrylamide hydrogel.[56] Of note, the tetrahedron assembly process was extremely fast with a high yield of 85%, indicating that the additional sequences and amino groups did not significantly affect the assembly.

Detection Principle of the ECL biosensor. The schematic diagram of the constructed biosensor was illustrated in Scheme 1. ECL responses after each fabricated procedure were shown in Figure 3A. After the deposit of chitosan-RuSi NPs on GCE (curve a, black line), GA was introduced to activate the amino groups at the electrode surface and provided a reaction site for the subsequent immobilization of TD. Here, the TD scaffold was composed of a pendant stem-loop structure at one vertex (hairpin 1) and three aminol groups at the other three vertices. The aminol groups acted as anchors to react covalently with the aldehyde groups of GA, leading to the strong and rigid fixing of DNA tetrahedron. At the TD assembly process, no obvious ECL signal change was observed (curve b, orange line). The stem-loop structure of TD had two regions, one of which hybridized to the target miRNA and the other hybridized to the signaling probe. In our design, prostate cancer related biomarker-miRNA141 was incubated to open the stem-loop structure of TD and the obtained ECL signal showed a minor decrease because the enhanced steric effects of BSA protein and DNA scaffolds blocked the electron transfer in the ECL process (curve c, pink line). Gold nanocages modified with stem-loop hairpin 2 (tDNA-Au

nanocages) were then introduced and acted as the signaling probe. The hairpin 2 could combined with the rest part of the hairpin 1 and competed with the hybridized miRNA which contributed to the release of target miRNA. The free miRNA was reused in subsequent DNA hybridization cycles and the ECL quenching signal was amplified which increased the sensitivity of the biosensor (curve d, blue line). In our design, the quenching efficiency was highly depended on the concentration of the target miRNA. At the concentration of 10 pM target miRNA, ECL signal could be significantly quenched by 78.4% due to the well overlap between the absorption spectrum of gold nanocages and the emission spectrum of RuSi NPs (Figure 3B, b). If target miRNA was absent in the assembly process, the hairpin of TD was in a "closed" state and could not react with the subsequent hairpin 2. As shown in Figure 3(B, a), no ECL signal quenching was observed.

Comparison of different sensing interface. In the electrochemical sensing process, the sensing interface played an important role. Most of the traditional electrochemical biosensor used the single strand DNA to construct the sensing interface. However, it had several limitations in signal responses and detection sensitivity compared with the recent developed TD electrochemical biosensor. Here, to explore the signal difference of the two kinds of sensing interface and discover whether the phenomenon also existed in the ECL detection process, we compared the TD-based interface with the traditional single strand DNA (ssDNA)-based interface through measuring the ECL quenching efficiency of assembled Au nanocages to the substrate RuSi NPs and the results were shown in Figure 4A. At the concentrations of 0.1 pM target miRNA,

TD-based biosensor exhibited obvious quenching (43.2%) while the ssDNA-based biosensor showed only slight signal quenching (8.8%), demonstrating the superior performance of the TD in the construction of the ECL biosensor. In addition, we did the comparison in different concentrations of target miRNA probes from 0.1 pM to 10 pM. As seen in Figure 4B, at each concentrations, TD-based sensing interface all exhibited better performance than that of ssDNA. We speculated that the obtained results was mainly due to the "size dilemma" of the ssDNA based ECL sensing interface.[57] For the interface with ssDNA, the single strand probes tended to lie flat at the electrode surface which resulted in the disorderly and unsystematic arrangement. As a result, the electrode steric hindrance increased which decreased the binding efficiency due to the reduced probability of collision of the target miRNA probes. As a contrast, TD based interface showed a high-ordered probe arrangement and upright orientation which was high efficient for DNA hybridization.

To demonstrate the superiority of the Au nanocages in the construction of biosensor, we took the gold nanoparticles (AuNPs) with average size of 18 nm into comparison. The AuNPs were used to replace the Au nanocages in the electrode assembly process. TEM image showed that the synthesized AuNPs possessed good homogeneity (Figure 4C). The tDNA probe was grafted onto AuNPs with the same method as Au nanocages and the obtained tDNA-AuNPs nanocomposite was used as the signal probe. As seen in Figure 4D, after sandwich DNA structure modified GCE was incubated with tDNA-AuNPs (c), the ECL signal decreased and the quenching efficiency was 21.0% which was much lower than that of Au nanocages (b). Thus, the

Au nanocages used in the biosensor showed superior performance than AuNPs.

We postulated that the difference of signal responses between Au nanocages and AuNPs came from two parts, overlap degree of the spectra between the ECL donor-acceptor pairs and the UV-vis absorption intensity. Firstly, we did UV-vis measurement of the two types of Au nanomaterials with the same size and the result was shown in Figure 1D. The concentration of the analytes was kept the same at 0.5 mg/mL. It can be seen that the absorption peak of the Au nanocages was 628 nm which perfectly overlapped with the ECL emission spectra of RuSi while the peak of the AuNPs was 521 nm and exhibited a weak absorption at 620 nm. Meanwhile, the Au nanocages showed a stronger absorbance (curve a) than that of AuNPs (curve c). The UV-vis results confirmed the superior performance of Au nanocages in plasma resonance absorption which contributed to the significant quenching of the ECL signal.

Optimization of the experiment conditions. For the better performance of the target miRNA detection, the experiment conditions including the doped content of $Ru(bpy)_3^{2+}$ in RuSi NPs, the concentration of RuSi NPs, TD, TprA and tDNA linked to Au nanocages were optimized. The influence of the doped content of $Ru(bpy)_3^{2+}$ in RuSi NP on the ECL performance was firstly measured. We changed the added concentrations of $Ru(bpy)_3^{2+}$ in the fabrication process of RuSi NPs from 5 mM to 60 mM to regulate the $Ru(bpy)_3^{2+}$ doped content. As seen in Figure S2, with the concentrations of the added $Ru(bpy)_3^{2+}$ increasing from 5 mM to 40 mM, the ECL intensity on the obtained RuSi modified electrodes enhanced quickly and became

stable after the concentrations of $Ru(bpy)_3^{2+}$ reached to 40 mM. To evaluate the effects of the $Ru(bpy)_3^{2+}$ doped content on the detection limit and linear range of the biosensor, we selected two kinds of RuSi NPs fabricated with 10 mM and 40 mM $Ru(bpy)_3^{2+}$, for comparative study. The corresponding doped contents of $Ru(bpy)_3^{2+}$ in the two kinds of RuSi NPs were calculated to be 1.73×10^4 and 6.59×10^4 molecules per NP, respectively (shown in supporting information). As revealed in Table S2, at high doped content of $Ru(bpy)_3^{2+}$, the biosensor exhibited a lower detection limit than that of low doped content and a comparable linear range. Thus, the RuSi NPs fabricated with 40 mM $Ru(bpy)_3^{2+}$ was selected in the following experiments.. The concentrations of dropped RuSi NPs on the electrode surface were studied. As shown in Figure S3A, the ECL signal enhanced with the increasing of concentrations from 0.5 mg/mL to 4.0 mg/mL, and decreased from 4.0 mg/mL to 10.0 mg/mL due to the steric effects caused by the increased thickness of the deposited nanoparticles film. Thus, 4.0 mg/mL was chosen in the following experiments. The concentrations of TprA was also investigated (Figure S3B). Increasing the concentrations from 5 mM to 25 mM, the ECL intensity enhanced quickly owning to the increasing interactions of the anion and cation radicals generated by $Ru(bpy)_3^{2+}$ and TprA. The ECL signal became stable while the concentration of TprA was higher than 25 mM because the excess TprA radicals tended to collide and annihilate with each other at the outer surface of the RuSi NPs. Therefore, 25 mM was selected as the optimal concentration. The effect of TD concentration was shown in Figure S3C. It was found that the ECL quenching efficiency increased with the concentration of TD

increasing and achieved the optimization at the concentration of 2 μM. ECL increment became stable when furtherly increasing the concentrations of TD. The concentration of tDNA linked to the Au nanocages (0.5 mg/mL) was studied as well. As seen in Figure S3D, when the concentrations of tDNA increased from 0.5 μM to 5.0 μM, the ECL quenching obviously increased due to the increasing amount of Au nanocages on the electrode surface. Furtherly increasing the concentration of tDNA led to slightly decrease of the quenching efficiency because of the decreased hybridization efficiency caused by the "crowd effect" of the tDNA strand.[58] Hence, 5.0 μM was chosen as the optimal concentration of tDNA.

Detection of miRNA141. Taking advantages of the high-efficient ECL-RET, a signal off biosensing platform was constructed for the detection of the miRNA141. As demonstrated above, after target miRNA was introduced onto the electrode, the ECL signal dramatically decreased due to miRNA induced assembly of the Au nanocages signal probe. Figure 5A illustrated the ECL responses of the biosensor toward different concentrations of miRNA. The corresponding standard curve for miRNA detection was shown in Figure 5B. A good linear relationship between the miRNA concentration and the logarithm of ECL intensity increment ($\Delta I=I_0-I$) was obtained in the concentration range of 1.0 fM to 10 pM (Figure 5B, inset). The linear fitting equation was $\Delta I=0.101\lg c+1.575$ with a correlation coefficient of 0.996 (c represents the concentration of miRNA, M). The limit of detection (LOD) was estimated to be 0.4 fM at signal-to-noise ratio S/N=3. We compared the performances between the proposed biosensor and other miRNA biosensors. As shown in Table S3, the proposed

biosensor exhibited a higher sensitivity with a lower detection limit, which was attributed to the DNA circle amplification and highly quenching efficiency of the Au nanocages.

Stability and selectivity of the ECL biosensor. ECL stability of the biosensor was examined by monitoring the ECL response of RuSi NPs modified GCE under consecutive cyclic voltammetry scans for 20 cycles. As seen in Figure 5C, the ECL signal showed no obvious changes, suggesting the acceptable stability of the proposed biosensor. Selectivity of the biosensor was evaluated by comparing the ECL intensity increment ($\triangle$I) to different kinds of miRNA sequences (10 pM), including completely complementary miRNA sequence (miRNA141), single-base miRNA sequence, two-base mismatched miRNA sequence (miRNA200a), non-complementary miRNA sequence (miRNA21) and the mixture of these sequences. As shown in Figure 5D, in the presence of non-complementary miRNA (a, miRNA21), ECL signal exhibited scarcely decrease. When two-base (b, miRNA200a) or single-base mismatched miRNA (c) existed, the signal of $\triangle$I was slightly increased but still much lower than that of the complementary target miRNA141 (d). The ECL increment of the mixture of these sequences (e) exhibited almost the same as the complementary sequence. These results suggested the acceptable selectivity of the proposed ECL biosensor.

Real Sample Analysis. The practical utility of the proposed ECL biosensor for detecting real samples was evaluated by determining spiked miRNA141 samples with different concentrations. The samples were prepared by adding miRNA141 solution to 10% diluted normal human serum. As shown in Table 1, the results exhibited good

recoveries from 97% to 106% and RSDs from 3.7% to 5.5%, which suggested that the developed method has potential for determination of miRNA141 in clinical analysis.

CONCLUSION

In summary, we developed an efficient ECL-RET system between RuSi NPs and hollow Au nanocages for the sensitive and specific detection of miRNA141. The constructed TD-based interface showed superior performance in the signal responses of ECL-RET system than that of the conventional ssDNA-based interface. Compared with solid Au nanospheres, the plasmon band of hollow Au nanocages showed stronger absorbance and better overlapping with the ECL emission spectra of RuSi NPs, which contributed to the higher energy transfer efficiency in the ECL-RET. Hairpin based DNA sandwich assay and the subsequent cyclic DNA amplification could greatly increase the detection sensitivity of the ECL-RET system with a detection limit at the fetomolar level. It is believed that this study could offer a perspective for the rational use of various SPR nanostructures for innovative ECL sensors.

ASSOCIATED CONTENT

Supporting Information

Reagents and apparatus, FDTD simulations of Au nanocages, the influence of $Ru(bpy)_3^{2+}$ doped content on the sensor performance, optimization of the experiment parameters and comparison with other reported miRNA detection methods. The Supporting Information is available free of charge on the ACS Publications website at

DOI: 10.1021/.

AUTHOR INFORMATION

Corresponding Authors

*Tel/Fax: +86-25-83597294. E-mail: weizhao@nju.edu.cn, xujj@nju.edu.cn.

Notes

The authors declare no competing financial interest.

ACKNOWLEDGMENT

We gratefully acknowledge the National Key R&D Program of China (Grant 2016YFA0201200), the National Natural Science Foundation of China (Grants Nos. 21475058, and 21605079), and Natural Science Foundation of Jiangsu Province (BK20160637). This work was also supported by a Project Funded by the Priority Academic Program Development of Jiangsu Higher Education Institutions and the Fundamental Research Funds for the Central Universities.

REFERENCES

(1) Zeng, J.; Zhang, Q.; Chen, J. Y.; Xia, Y. N. *Nano Lett.* **2010**, *10*, 30-35.

(2) Lee, J. S.; Ulmann, P. A.; Han, M. S.; Mirkin, C. A. *Nano Lett.* **2008**, *8*, 529-533.

(3) Zeng, J.; Huang, J. L.; Lu, W.; Wang, X. P.; Wang, B.; Zhang, S. Y.; Hou, J. G. *Adv. Mater.* **2007**, *19*, 2172-2176.

(4) Huff, T. B.; Tong, L.; Zhao, Y.; Hansen, M. N.; Cheng, J. X.; Wei, A. *Nanomedicine* **2007**, *2*, 125-132.

(5) Gobin, A. M.; Lee, M. H.; Halas, N. J.; James, W. D.; Drezek, R. A.; West, J. L. *Nano Lett.* **2007**, *7*, 1929-1934.

(6) Zou, S. L.; Schatz, G. C. *Chem. Phys. Lett.* **2005**, *403*, 62-67.

(7) Oldenburg, S. J.; Averitt, R. D.; Westcott, S. L.; Halas, N. J. *Chem. Phys. Lett.* **1998**, *288*, 243-247.

(8) Wang, H.; Daniel, W., B.; Peter, N.; Naomi, J., H. *Acc. Chem. Res.* **2007**, *40*, 53-62.

(9) Zhao, J.; Pinchuk, A. O.; McMahon, J. M.; Li, S. Z.; Ausman, L. K.; Atkinson, A. L.; Schatz, G. C. *Acc. Chem. Res.* **2008**, *41*, 1710-1720.

(10) Tabor, C.; Murali, R.; Mahmoud, M.; El-Sayed, M. A. *J. Phys. Chem. A* **2009**, *113*, 1946-1953.

(11) Storhoff, J. J.; Lazarides, A. A.; Mucic, R. C.; Mirkin, C. A.; Letsinger, R. L.; Schatz, G. C. *J. Am. Chem. Soc.* **2000**, *122*, 4640-4650.

(12) Mock, J. J.; Smith, D. R.; Schultz, S. *Nano Lett.* **2003**, *3*, 485-491.

(13) El-Sayed, I. H.; Huang, X. H.; El-Sayed, M. A. *Nano Lett.* **2005**, *5*, 829-834.

(14) Sih, B. C.; Wolf, M. O. *J. Phys. Chem. B* **2006**, *110*, 22298-22301.

(15) Chen, H. J.; Kou, X. S.; Yang, Z.; Ni, W. H.; Wang, J. F. *Langmuir* **2008**, *24*, 5233-5237.

(16) Chen, J. Y.; Wiley, B.; Li, Z. Y.; Campbell, D.; Saeki, F.; Cang, H.; Au, L.; Lee, J.; Li, X. D.; Xia, Y. N. *Adv. Mater.* **2005**, *17*, 2255-2261.

(17) Hu, M.; Chen, J. Y.; Li, Z. Y.; Au, L.; Hartland, G. V.; Li, X. D.; Marquez, M.; Xia, Y. N. *Chem. Soc. Rev.* **2006**, *35*, 1084-1094.

(18) Mahmoud, M. A.; Snyder, B.; El-Sayed, M. A. *J. Phys. Chem. C* **2010**, *114*, 7436-7443.

(19) Skrabalak, S. E.; Chen, J. Y.; Sun, Y. G.; Lu, X. M.; Au, L.; Cobley, C. M.; Xia, Y. N. *Acc. Chem. Res.* **2008**, *41*, 1587-1595.

(20) Mahmoud, M. A.; El-Sayed, M. A. *J. Phys. Chem. C* **2008**, *112*, 14618-14625.

(21) Mackey, M. A.; Saira, F.; Mahmoud, M. A.; El-Sayed, M. A. *Bioconjug. Chem.* **2013**, *24*, 897-906.

(22) Wang, Y. C.; Black, K. C. L.; Luehmann, H.; Li, W. Y.; Zhang, Y.; Cai, X.; Wan, D. H.; Liu, S. Y.; Li, M.; Kim, P.; Li, Z. Y.; Wang, L. H. V.; Liu, Y. J.; Xia, Y. N. *ACS Nano* **2013**, *7*, 2068-2077.

(23) Robinson, R.; Gerlach, W.; Ghandehari, H. *J. Controlled Release* **2015**, *220*, 245-252.

(24) Xue, W. L.; Luo, L. Y.; Li, Y. J.; Yin, T.; Bian, K. X.; Zhu, R. Y.; Gao, D. W. *J. Mater. Chem. B* **2017**, *5*, 5641-5647.

(25) Wang, H. F.; Han, J.; Lu, W. S.; Zhang, J. P.; Li, J. R.; Jiang, L. *J. Colloid Interface Sci.* **2015**, *440*, 236-244.

(26) Wu, M. S.; He, L. J.; Xu, J. J.; Chen, H. Y. *Anal. Chem.* **2014**, *86*, 4559-4565.

(27) Wu, M. S.; Shi, H. W.; He, L. J.; Xu, J. J.; Chen, H. Y. *Anal. Chem.* **2012**, *84*, 4207-4213.

(28) Wu, M. S.; Shi, H. W.; Xu, J. J.; Chen, H. Y. *Chem. Commun.* **2011**, *47*, 7752-7754.

(29) Li, Z. X.; Zhou, Y. Q.; Yan, D. P.; Wei, M. *J. Mater. Chem. C* **2017**, *5*,

3473-3479.

(30) Zhou, Y. Q.; Yan, D. P.; Wei, M. *J. Mater. Chem. C* **2015**, *3*, 10099-10106.

(31) Fan, G. L.; Yan, D. P. *Adv. Opt. Mater.* **2016**, *4*, 2139-2147.

(32) Tian, R.; Zhang, S. T.; Li, M. W.; Zhou, Y. Q.; Lu, B.; Yan, D. P.; Wei, M.; Evans, D. G.; Duan, X. *Adv. Funct. Mater.* **2015**, *25*, 5006-5015.

(33) Chen, X. Q.; Gui, W. Y.; Ma, Q. *Anal. Chim. Acta* **2018**, *1009*, 73-80.

(34) Li, M. X.; Feng, Q. M.; Zhou, Z.; Zhao, W.; Xu, J. J.; Chen, H. Y. *Anal. Chem.* **2018**, *90*, 1340-1347.

(35) Dong, Y. P.; Zhou, Y.; Wang, J.; Zhu, J. J. *Anal. Chem.* **2016**, *88*, 5469-5475.

(36) Ma, H. M.; Li, X. J.; Yan, T.; Li, Y.; Liu, H. Y.; Zhang, Y.; Wu, D.; Du, B.; Wei, Q. *ACS Appl. Mater. Interfaces* **2016**, *8*, 10121-10127.

(37) Zhu, W. J.; Khan, M. S.; Cao, W.; Sun, X.; Ma, H. M.; Zhang, Y.; Wei, Q. *Biosens. Bioelectron.* **2018**, *99*, 346-352.

(38) Sun, F.; Wang, Z. Y.; Feng, Y. Q.; Cheng, Y. X.; Ju, H. X.; Quan, Y. W. *Biosens. Bioelectron.* **2018**, *100*, 28-34.

(39) Ke, H.; Sha, H. F.; Wang, Y. F.; Guo, W. W.; Zhang, X.; Wang, Z. M.; Huang, C. S.; Jia, N. Q. *Biosens. Bioelectron.* **2018**, *100*, 266-273.

(40) Babamiri, B.; Salimi, A.; Hallaj, R. *Biosens. Bioelectron.* **2018**, *102*, 328-335.

(41) Liu, C.; Wang, L.; Lu, L. P.; Kang, T. F. *Anal. Methods* **2017**, *9*, 6760-6768.

(42) Fu, X. M.; Yang, Y.; Wang, N.; Chen, S. H. *Sens. Actuators, B* **2017**, *250*, 584-590.

(43) Zhou, H.; Liu, J.; Xu, J. J.; Chen, H. Y. *Chem. Commun.* **2011**, *47*, 8358-8360.

(44) Shan, Y.; Xu, J. J.; Chen, H. Y. *Chem. Commun.* **2009**, *45*, 905-907.

(45) Zhou, H.; Zhang, Y. Y.; Liu, J.; Xu, J. J.; Chen, H. Y. *J. Phys. Chem. C* **2012**, *116*, 17773–17780.

(46) Sepúlveda, B.; Angelomé, P. C.; Lechuga, L. M.; Liz-Marzán, L. M. *Nano Today* **2009**, *4*, 244-251.

(47) Chen, J.; Wang, D.; Xi, J.; Au, L.; Siekkinen, A.; Warsen, A.; Li, Z. Y.; Zhang, H.; Xia, Y.; Li, X. *Nano Lett.* **2007**, *7*, 1318-1322.

(48) Lin, M. H.; Wang, J. J.; Zhou, G. B.; Wang, J. B.; Wu, N.; Lu, J. X.; Gao, J. M.; Chen, X. Q.; Shi, J. Y.; Zuo, X. L.; Fan, C. H. *Angew. Chem. Int. Ed.* **2015**, *54*, 2151-2155.

(49) Wu, M. S.; Qian, G. S.; Xu, J. J.; Chen, H. Y. *Anal. Chem.* **2012**, *84*, 5407-5414.

(50) Wei, H.; Liu, J. F.; Zhou, L. L.; Li, J.; Jiang, X. E.; Kang, J. Z.; Yang, X. R.; Dong, S. J.; Wang, E. K. *Chem. - Eur. J.* **2008**, *14*, 3687-3693.

(51) Chen, X. Q.; Zhou, G. B.; Song, P.; Wang, J. J.; Gao, J. M.; Lu, J. X.; Fan, C. H.; Zuo, X. L. *Anal. Chem.* **2014**, *86*, 7337-7342.

(52) Jia, X. F.; Yang, X. A.; Li, J.; Liab, D. Y.; Wang, E. K. *Chem. Commun.* **2014**, *50*, 237-239.

(53) Xu, S. M.; Yuan, H.; Xu, A.; Wang, J.; Wu, L. J. *Langmuir* **2011**, *27*, 13629-13634.

(54) Lu, H. J.; Zhao, W.; Xu, J. J.; Chen, H. Y. *Biosens. Bioelectron.* **2018**, *102*, 624-630.

(55) Goodman, R. P.; Schaap, I. A.; Tardin, C. F.; Erben, C. M.; Berry, R. M.; Schmidt,

C. F.; Turberfield, A. J. *Science* **2005**, *310*, 1661-1665.

(56) Goodman, R. P.; Berry, R. M.; Turberfield, A. J. *Chem. Commun.* **2004**, 1372-1373.

(57) Lin, M. H.; Wen, Y. L.; Li, L. Y.; Pei, H.; Liu, G.; Song, H. Y.; Zuo, X. L.; Fan, C. H.; Huang, Q. *Anal. Chem.* **2014**, *86*, 2285-2288.

(58) Ge, Z. L.; Lin, M. H.; Wang, P.; Pei, H.; Yan, J.; Sho, J. Y.; Huang, Q.; He, D. N.; Fan, C. H.; Zuo, X. L. *Anal. Chem.* **2014**, *86*, 2124-2130.

Scheme, Figures & Table:

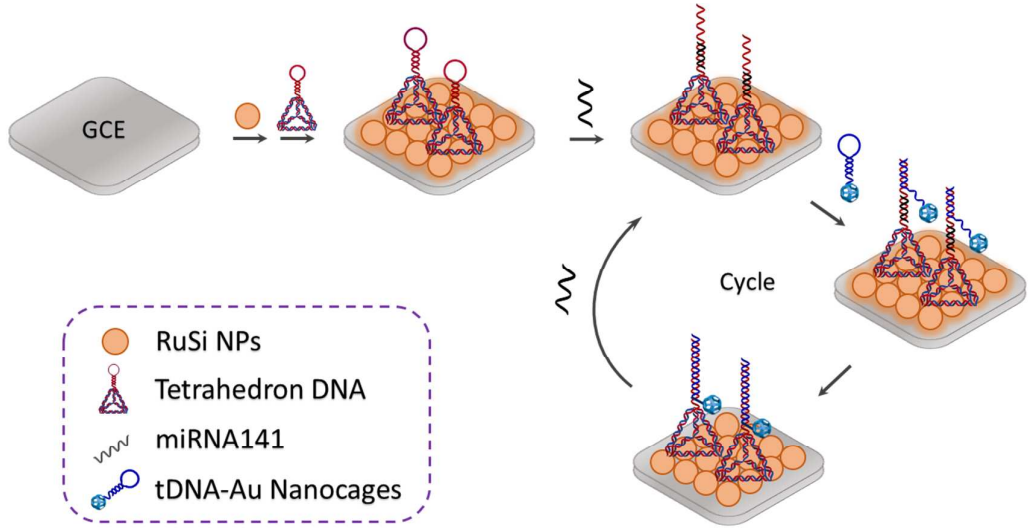

Scheme 1. Schematic illustration of the structure and modification process of the ECL biosensor

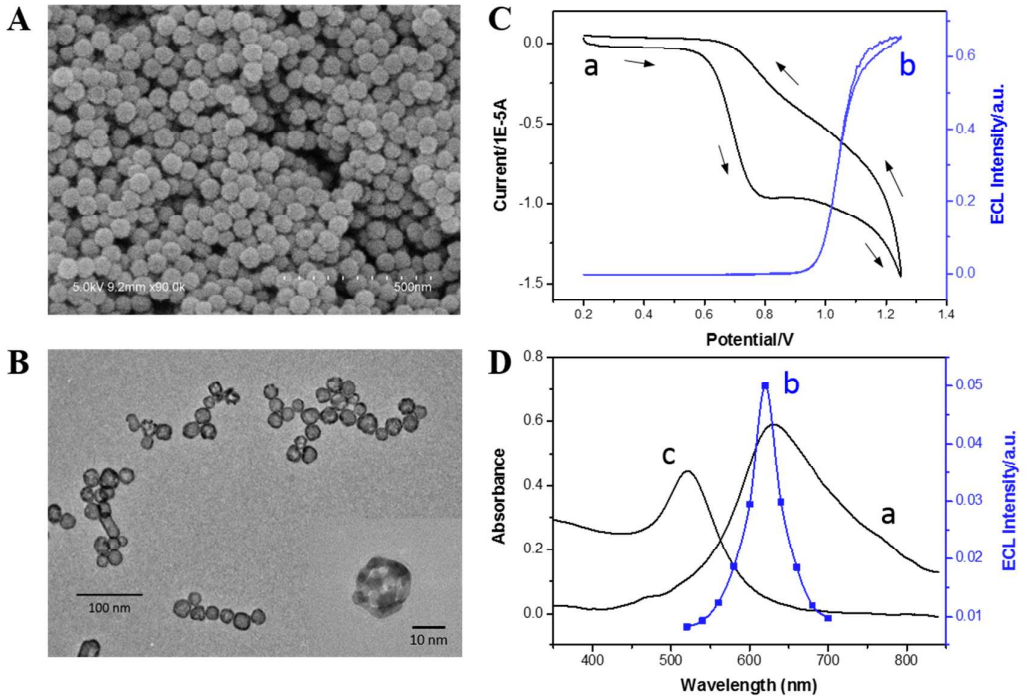

Figure 1. (A) SEM image of RuSi NPs. Scale bar: 500 nm (B) TEM image of the Au nanocages. Scale bar: 100 nm. Inset：Magnified TEM image of an Au nanocage. Scale bar: 10 nm. (C) The cyclic voltammetry curve of the GCE/RuSi NPs (a, black line) and ECL-potential curve of the GCE/RuSi NPs (b, blue line). The black arrows represent the scanning direction. ECL detection buffer: 0.1 M PBS (pH 7.4) containing 25 mM TprA. (D) Uv-vis absorption spectrum of Au nanocages (a, black line) and 18-nm AuNPs (c, black line); ECL emission spectrum of RuSi NPs (b, blue line) obtained through optical fiters under as cyclic potential scan from 0 to 1.25 V. ECL detection buffer: 0.1 M PBS (pH 7.4) containing 25 mM TprA.

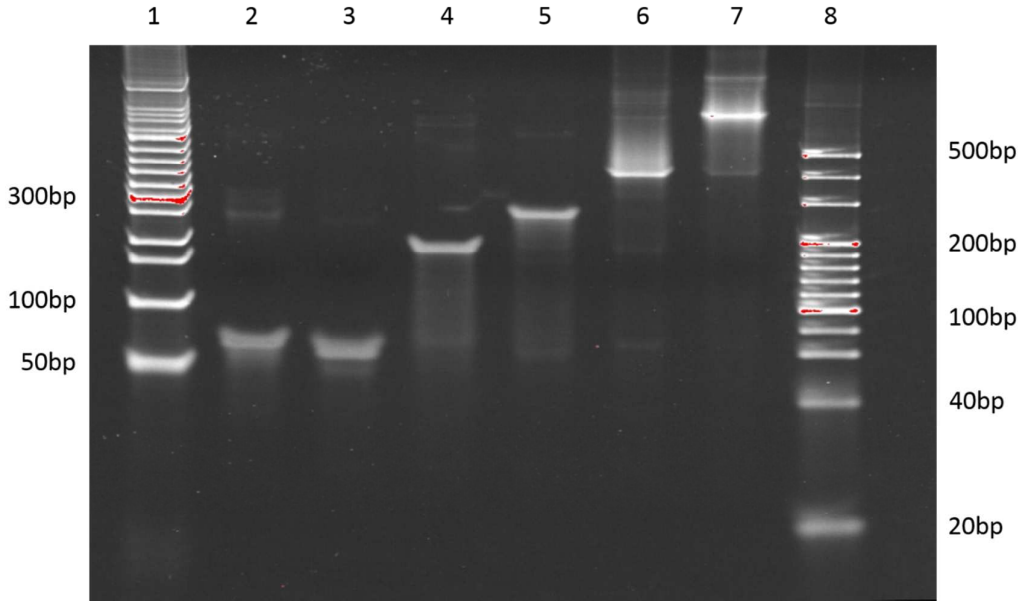

Figure 2. Gel electrophoresis image of different structures. Lane 2: S2, Lane 3: S3, Lane 4: S2S3, Lane 5: S1S2, Lane 6: S1S2S3, Lane 7: S1S2S3S4 (TD), Lane 1: 50 bp DNA marker, Lane 8: 20 bp DNA marker (purchased from TaKaRa).

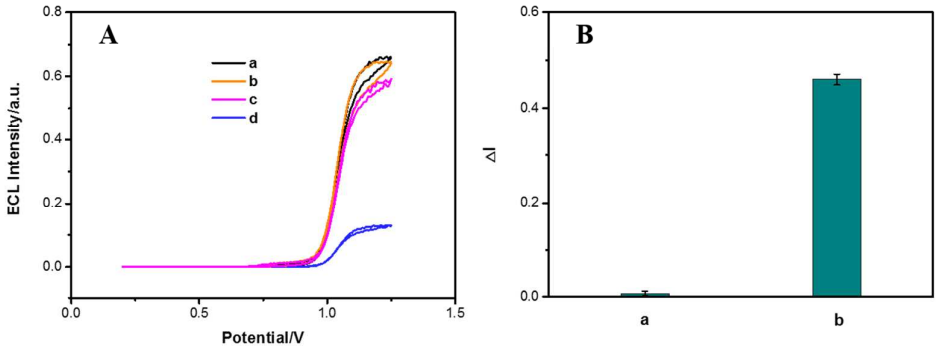

Figure 3. (A) ECL signals of GCE at different stages: (a) GCE/RuSi; (b) GCE/RuSi/TN; (c) GCE/RuSi/TN/BSA/miRNA141; (d) GCE/RuSi/TN/BSA/miRNA141/Au nano-cages; The concentration of target miRNA141 was 10 pM; ECL detection buffer: 0.1 M PBS containing 25 mM TprA; (B) ECL signal increment (ΔI) of GCE in the absence (a) and presence (b) of target miRNA-141 (10 pM); $\Delta I=I_0-I$; I_0 means the original ECL intensity while I represents the ECL intensity after incubated with Au nanocages;

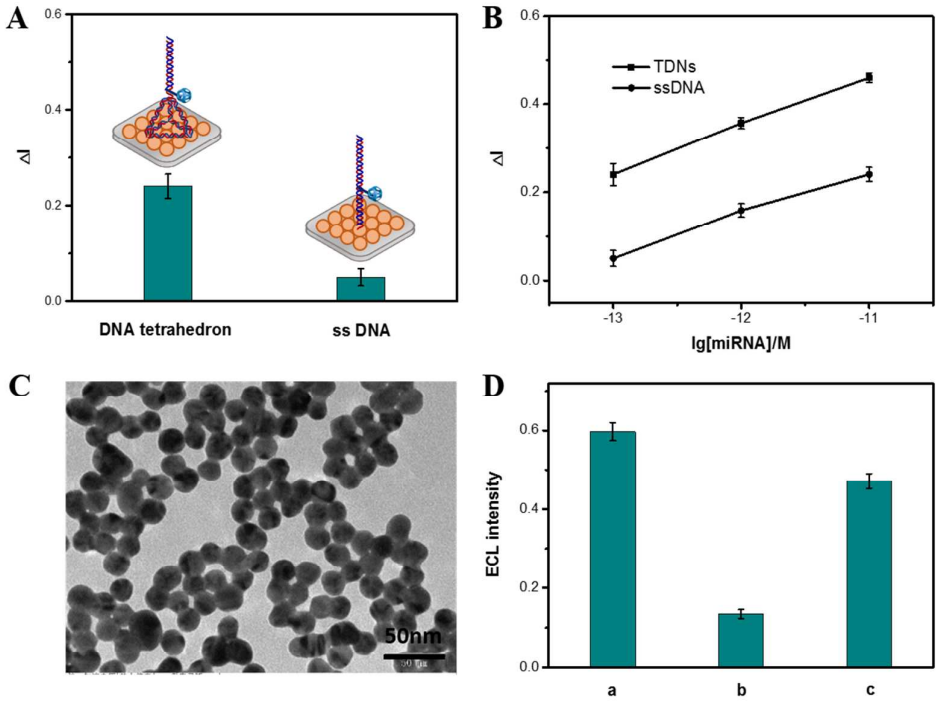

Figure 4. (A) ECL quenching efficiency of the tetrahedron based assay and ssDNA based assay, respectively. The concentration of the target miRNA was 0.1 pM. (B) ECL quenching curves of the tetrahedron (upper curve) and ssDNA (below curve) based assay at different concentrations of target miRNA. (C) TEM image of 18 nm AuNPs. Scale bar: 50 nm. (D) ECL intensity of GCE under different modification states: (a) GCE/RuSi/TN/BSA/ miRNA141; (b) GCE/RuSi/TN/BSA /miRNA141/Au nanocages; (c) GCE/RuSi/TN/ BSA /miRNA141/AuNPs; ECL detection buffer: 0.1 M PBS containing 25 mM TprA;

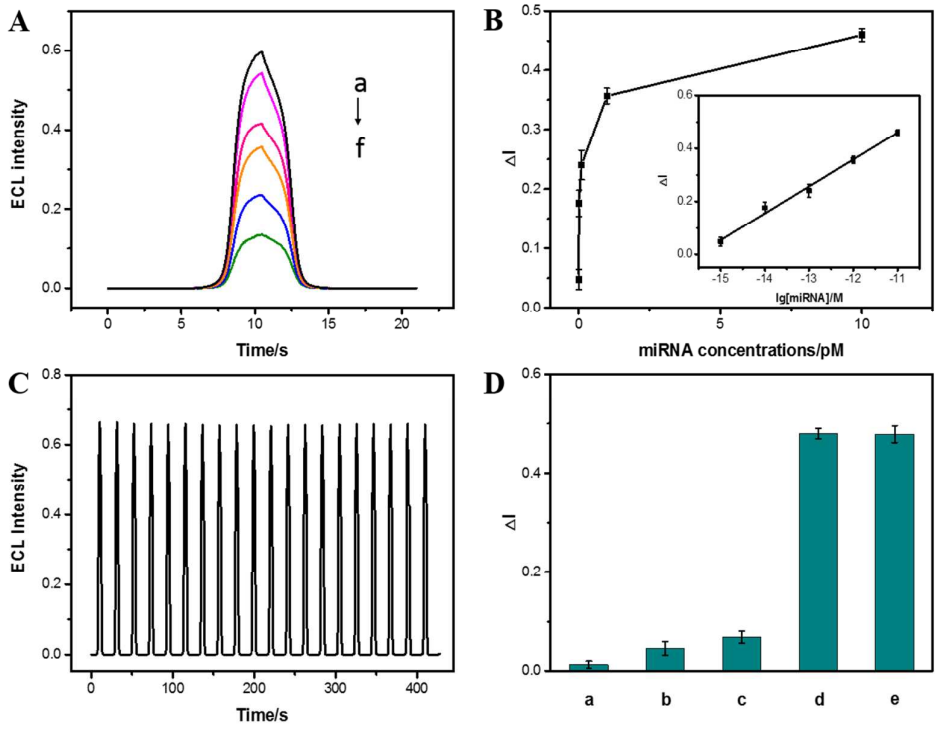

Figure 5. (A) ECL signals of the biosensor incubated with different concentrations of target miRNA (from a to f, 0 M, 1 fM, 10fM, 0.1 pM, 1 pM, 10 pM, respectively). (B) ECL signal quenching of the biosensor incubated with different concentrations of target miRNA (from left to right, 1 fM, 10fM, 0.1 pM, 1 pM, 10 pM). Inset: linear relationship between ECL-RET efficiency and the logarithm of target miRNA concentration, three measurements for each point. (C) ECL stability of the GCE-RuSi-CS under consecutive scans for 20 cycles. (D) ECL signal quenching after incubated with non-complementary sequence (miRNA21, a), two-base mismatched sequence (miRNA200a, b), single-base mismatched sequence (c), target miRNA (miRNA141, d) and the mixture of these sequences (e). $\Delta I=I_0-I$ (I_0 means the origin ECL intensity, while I represents the ECL intensity after incubated with miRNAs).

Table 1. Recovery tests for miRNA-141 in spiked human serum samples (n=3).

Samples	Added	Found	RSD (%)	Recovery (%)
1	1.0 fM	1.06 fM	4.9	106
2	10.0 fM	10.1 fM	5.5	101
3	100 fM	99 fM	4.2	99
4	1.0 pM	0.97 pM	3.7	97
5	10.0 pM	10.3 pM	3.8	103

Table of Contents